



Plasma-catalytic CO₂ hydrogenation to methanol over CuO-MgO/Beta catalyst with high selectivity

Qian Chen^{a,1}, Shengyan Meng^{a,1}, Rui Liu^a, Xiaohan Zhai^b, Xinkui Wang^a, Li Wang^b, Hongchen Guo^a, Yanhui Yi^{a,*}

^a State Key Laboratory of Fine Chemicals, School of Chemical Engineering, Dalian University of Technology, Dalian 116024, PR China

^b College of Environmental Sciences and Engineering, Dalian Maritime University, Dalian 116026, Liaoning, PR China

ARTICLE INFO

Keywords:

CO₂ hydrogenation
Methanol production
Cu-based catalysts
MgO promoter
Plasma catalysis

ABSTRACT

Herein, we report a CuO-MgO/Beta catalyst, which exhibits 72.0% methanol selectivity with 8.5% CO₂ conversion in plasma-catalytic CO₂ hydrogenation at ambient conditions (30 °C and 0.1 MPa). The catalysts have been systematically characterized by XRD, H₂-TPR, HRTEM, STEM, XPS, CO₂-TPD and NH₃-TPD to study the interaction between CuO and MgO, as well as physicochemical properties of the catalysts. Furthermore, in-situ Optical Emission Spectroscopy (OES) and in-situ Fourier Transform Infrared Spectroscopy (FTIR) were employed to investigate the active species in gas-phase and on catalyst surface. The excellent selectivity of the CuO-MgO/Beta catalyst is attributed to synergy between MgO and CuO species. The strong interaction between CuO and MgO leads to electron transfer from MgO to CuO, which is favorable for partially reduction of CuO to form Cu₂O active sites. Furthermore, MgO strongly adsorb CO₂ to form formate species, which suppresses CO generation and leads to CO₂ hydrogenation through Formate pathway for CH₃OH production.

1. Introduction

The concentration of carbon dioxide (CO₂) in the atmosphere has reached 420 ppm, which brings the problem of global warming, seriously affecting normal life of human beings. While, the acceptable concentration of CO₂ in the atmosphere should be below 350 ppm. Thus, controlling the emissions of CO₂ is an important challenge for human beings to cope with the global warming [1]. Carbon dioxide capture and utilization (CCU) and carbon dioxide capture and storage (CCS) technologies have been proposed as feasible strategies to deal with this crisis. CCU is a technology that collects and converts CO₂ into valuable chemicals such as methanol, ethanol, methane, olefins, aromatics, urea, etc [2]. CO₂ hydrogenation to methanol using green hydrogen, therefore, has attracted much attention in recent years, since methanol is widely used as an important organic solvent, a crucial organic feedstock for organic synthesis (formaldehyde, dimethyl carbonate, ethylene, aromatics, acetic acid, etc.) and an energy source for fuel cell and gasoline [3].

CO₂ hydrogenation to methanol has been extensively studied, and excellent methanol selectivity has been obtained. Using nano In₂O₃

catalyst, Dang et al. achieved 6.7% CO₂ conversion and 99.5% methanol selectivity at 270 °C and 5 MPa [4]. Wang et al. prepared a Cu-Ni bimetallic catalyst and obtained 7.9% CO₂ conversion and 98.7% methanol selectivity at 225 °C and 4 MPa [5]. Employing a Cu-ZnO/MgO catalyst, Guo et al. realized 7.6% CO₂ conversion and 91% methanol selectivity at 200 °C and 5 MPa [6]. These experimental data indicate that high methanol selectivity has been achieved through conventional heterogeneous catalysis. However, due to the thermodynamic stability of CO₂ molecule, the hydrogenation reaction is usually carried out at relative high temperature (> 200 °C) and pressure (> 4 MPa).

Plasma offers a unique approach to facilitate thermodynamically unfavorable chemical reactions at low temperatures [7–15]. In the plasma, energetic electrons can activate CO₂ and H₂ to produce various active species including ions, radicals and excited species. Furthermore, CO₂ hydrogenation to methanol is an exothermic reaction, and the character of low temperature in non-thermal plasma is favorable for the production of methanol [8,9]. Thus, plasma-catalysis, combination of plasmas and catalysts, has been employed to drive CO₂ hydrogenation at low temperature and atmospheric pressure. Particularly, methanation of

* Corresponding author.

E-mail address: yyanhui@dlut.edu.cn (Y. Yi).

¹ These authors contributed equally (shared first authors).

CO₂ driven by plasma-catalysis employing Co/CeZrO₄ [10], Ni/UiO-66 [11], and Ni-Fe/LDH [12] catalysts has been studied, achieving nearly 100% CH₄ selectivity with 70%, 85% and 72% CO₂ conversion, respectively. However, production of methanol by plasma-catalytic CO₂ hydrogenation has been less studied. Wang et al. [13] achieved 21.2% CO₂ conversion and 53.7% methanol selectivity using Cu/ γ -Al₂O₃ catalyst at 30 °C and 0.1 MPa. Cui et al. [14] obtained 10% CO₂ conversion and 47.5% methanol selectivity using Cu/ γ -Al₂O₃ catalyst at 60 °C and 0.1 MPa. Men et al. [15] gain 37% CO₂ conversion and 62.6% methanol selectivity using Pt/film/In₂O₃ catalyst at 30 °C and 0.1 MPa. That is, the selectivity of methanol in plasma-catalytic CO₂ hydrogenation is still much lower than that of conventional thermal catalysis.

Herein, we report a CuO-MgO catalyst using Beta zeolite as a support (CuO-MgO/Beta), which exhibits 72.0% methanol selectivity with 8.5% CO₂ conversion in plasma-catalytic CO₂ hydrogenation. The catalysts have been systematically characterized to study the interaction between CuO and MgO. Furthermore, in-situ Optical Emission Spectroscopy (OES) and in-situ Fourier Transform Infrared Spectroscopy (FTIR) were employed to investigate the active species in gas-phase and on catalyst surface, and thus the catalytic mechanism of CO₂ hydrogenation to methanol on CuO-MgO/Beta catalyst with high selectivity have been revealed.

2. Experimental

2.1. Catalyst preparation

The catalysts were prepared by two-step impregnation. Beta zeolite was purchased from Nankai University. Mg (NO₃)₂·6 H₂O and Cu (NO₃)₂·6 H₂O were purchased from Tianjin Kemiou Chemical Reagent Co., Ltd.

The MgO/Beta catalysts were prepared as follows. Initially, the precursor Mg (NO₃)₂·6 H₂O was measured to match the desired loading and added to beakers. Then, 4 g deionized water were added to the beakers, and the mixtures were stirred until uniform dispersion. Subsequently, 5 g Beta supporter was introduced into the solutions, and the mixtures were stirred for 15 min at room temperature. After that, the resulting mixtures were left to age for 12 h, and the samples were then subjected to a drying process by placing them in an oven at 110 °C for 12 h; Finally, the samples were transferred to a muffle furnace for calcination at 540 °C for 5 h, and the resulting samples were milled into powders to obtain the final MgO/Beta catalysts with different loadings.

For the preparation of CuO-MgO/Beta catalysts, the procedure mirrored that of MgO/Beta. Cu (NO₃)₂·6 H₂O precursor was measured to match the desired loading and added to beakers containing 4 g deionized water. The resulting solutions were stirred until homogeneous, and the pre-milled MgO/Beta samples were added into the solution. After 15 min of stirring at room temperature, the mixtures were allowed to age for 12 h. Finally, the CuO-MgO/Beta samples underwent drying at 110 °C for 12 h and calcination at 540 °C for 5 h.

2.2. Experimental setup and reaction evaluation

A schematic diagram of the experimental setup for the plasma-catalytic CO₂/H₂ reaction is shown in Fig. S1. A coaxial dielectric barrier discharge (DBD) reactor is used to generate CO₂/H₂ plasma. The DBD reactor consists of a pair of coaxial quartz cylinders (inner and outer quartz tubes) in which a stainless-steel (2 mm outer diameter) electrode is placed in the center, and circulating water is pumped into the space between the inner and outer cylinder, acting as a ground electrode. The discharge length is 60 mm, and the discharge gap is fully packed by catalyst granules (1.5 g, 0.85–0.42 mm diameter). CO₂ (18 ml/min) and H₂ (54 ml/min) are monitored by calibrated mass flow controllers.

The DBD reactor is connected to an AC high voltage power supply with a peak voltage up to 30 kV and a variable frequency ranging 7–12

kHz. The electrical signals (applied voltage, current and voltage on the external capacitor) are recorded by a four-channel digital oscilloscope (Tektronix, MDO 3024). The discharge power is calculated by using the Q-U Lissajous method. The discharge frequency is fixed at 9.2 kHz, and the applied power is maintained at around 24 W. The liquid product is collected by a cold trap at the exhaust of the DBD reactor.

A gas chromatograph (Tianmei 7900 equipped with a thermal conductivity detector and a TDX-01 column) is used to analyze the composition of the exhaust gases. The liquid products are quantitatively analyzed by another gas chromatograph (Shimadzu GC-2014 C equipped with a flame ionization detector and a PEG-20 M column). The variation of the gas volume is measured by a flow meter. The reaction temperature in the discharge area is close to the circulating water temperature (30 °C), while the temperature near the high-voltage electrode may be slightly higher than 30 °C.

To evaluate the reaction performance, the CO₂ conversion is calculated by Eq. (1):

$$X_{CO_2} = \frac{CO_{2[in]} - CO_{2[out]}}{CO_{2[in]}} \times 100\% \quad (1)$$

In the tail gas, only CO is detected by the gas chromatograph. The selectivity of CO is calculated by Eq. (2):

$$S_{CO} = \frac{CO_{[out]}}{CO_{2[in]} - CO_{2[out]}} \times 100\% \quad (2)$$

In the collected liquid, only one single product, CH₃OH, is detected by our gas chromatograph. Thus, the selectivity of CH₃OH is calculated by Eq. (3):

$$S_{CH_3OH} = 1 - S_{CO} \quad (3)$$

The energy consumption for CH₃OH generation is calculated by Eq. (4).

$$\text{energy consumption} \left(\frac{\text{kJ}}{\text{mmol}} \right) = \frac{\text{discharge power} \left(\frac{\text{J}}{\text{s}} \right)}{\text{rate of CH}_3\text{OH produced} \left(\frac{\text{mol}}{\text{s}} \right)} \times 10^{-6} \quad (4)$$

where the factor 10⁻⁶ accounts for the conversion of J/mol into kJ/mmole.

2.3. Catalyst characterization

X-ray diffraction (XRD) patterns are recorded on a SmartLab 9KW X-ray diffractometer using Cu K α radiation ($\lambda = 0.15406$ nm). The X-ray tube is operated at 240 kV and 50 mA. The data is recorded from 10° to 80° with 10°/min scanning speed and a step size of 0.02°. The elementary composition of the catalysts is determined by X-ray fluorescence spectroscopy (XRF) using X-ray fluorescence spectrometer (SRS 3400, Bruker, Germany). The specific surface area, pore volume, and pore size of the catalysts are measured by N₂ physisorption (Micromeritics ASAP 3020). Prior to the measurements, the catalysts are vacuum-treated at 350 °C for 5 h to remove impurities adsorbed in the catalyst pores. The scanning electron microscopy (SEM) is performed on a NOVA NanoSEM 450 electron microscope at 3 kV. The scanning transmission electron microscopy (STEM) and elementary mapping are performed on a JEM-ARM200F electron microscope at 200 kV. X-ray photoelectron spectroscopy (XPS) is conducted by Thermo Fisher ESCALAB XI+ with Al K α X-ray source. The binding energy values are calibrated using the C 1 s line at 284.8 eV as internal reference. The reduction properties of the catalysts are determined using H₂ temperature-programmed reduction (H₂-TPR) on a Quantachrome ChemBET Pulsar TPR apparatus. The samples (0.15 g) are purged for 1 h at 550 °C under a He atmosphere. After cooling to 50 °C, the samples are heated from 50 °C to 600 °C in an Ar-H₂ (120 ml/min, 10% H₂)

atmosphere at a rate of 10 °C/min, and the signal of H₂ consumption is collected. CO₂-TPD are performed on a Quantachrome ChemBET Pulsar TPR apparatus. The samples (0.15 g) are purged for 1 h at 550 °C under a He atmosphere. After cooling to 50 °C, the CO₂ is adsorbed in 80 min, and subsequently the samples are heated from 50 °C to 760 °C in an CO₂ (120 ml/min, 99.99% CO₂) atmosphere at a rate of 10 °C/min, and the signal of CO₂ consumption is collected. The ammonia temperature-programmed desorption (NH₃-TPD) is performed on a Quantachrome Chembet 3000 chemisorb instrument. Sample pellets (0.15 g, 0.42–0.85 mm) are loaded into a quartz U reactor and pretreated under helium flow at 600 °C for 1 h. Subsequently, the temperature is lowered to 100 °C in order to absorb ammonia for 30 min with a mixture of 5% NH₃ in He. After adsorption, the samples are cleaned for 30 min with 50 ml/min helium flow to remove physically adsorbed NH₃. Meanwhile, the desorption curve is recorded from 100 to 600 °C with a heating rate of 17 °C/min. Characterization of Cu species on the catalyst surface is performed by UV-Visible (UV-Vis) spectrophotometer (UV-550, Agilent, USA) with integrating sphere attachment (built-in dra2500).

In situ FTIR measurements were carried out using a FTIR spectrometer (Nicolet iS10, Thermo Scientific), equipped with a rapidly recoverable detector containing heavy hydrogen triethylene glycol salts (DTGS). The catalyst that was pressed into a wafer was packed into the reaction cell (Fig. S2) and pretreated in a CO₂/H₂ mixture (25 vol% CO₂, 75 vol% H₂) for 0.5 h before collecting the background. The plasma power was driven at 9.2 kHz with applied discharge voltage of 24 kV. The results were analyzed by the OMNIC software.

2.4. Plasma diagnostics

A Princeton Instruments ICCD spectrometer (SP 2758) with a 300 g/mm grating is used to in situ diagnose the CO₂/H₂ plasma (200–1100 nm). The slit width of the spectrometer is fixed at 20 μm, and the exposure time is fixed at 2 s. The waveforms of discharge voltage and discharge current are collected using a digital oscilloscope (DPO 3012, Tektronix, USA) with a high voltage probe (Tektronix P6015A) and a current probe (Pearson 6585), and the discharge power is calculated using the Lissajous curve.

3. Results and discussion

3.1. Catalytic performance

Fig. 1 shows the catalytic performance of CuO-MgO/Beta catalysts in plasma-catalytic CO₂ hydrogenation. As illustrated in Fig. 1A, in the case of “plasma only”, 3.3% CO₂ conversion is achieved with only 7.5% CH₃OH selectivity. After packing the CO₂/H₂ plasma with Beta support, the CO₂ conversion and CH₃OH selectivity increase to 4.8% and 44.8%, respectively. After replacing Beta support by MgO/Beta (with 15 wt% Mg loading), the reaction performance is slightly enhanced (5.0% CO₂ conversion and 49.8% CH₃OH selectivity), which means that MgO species can not catalyze the CO₂ hydrogenation reaction without assistance from some other active components. While, packing CO₂/H₂ plasma by CuO/Beta (with 10 wt% Cu loading) catalyst leads to an obvious enhancement of reaction performance, i.e., 6.8% CO₂ conversion and 59.8% CH₃OH selectivity, indicating that Cu species plays a

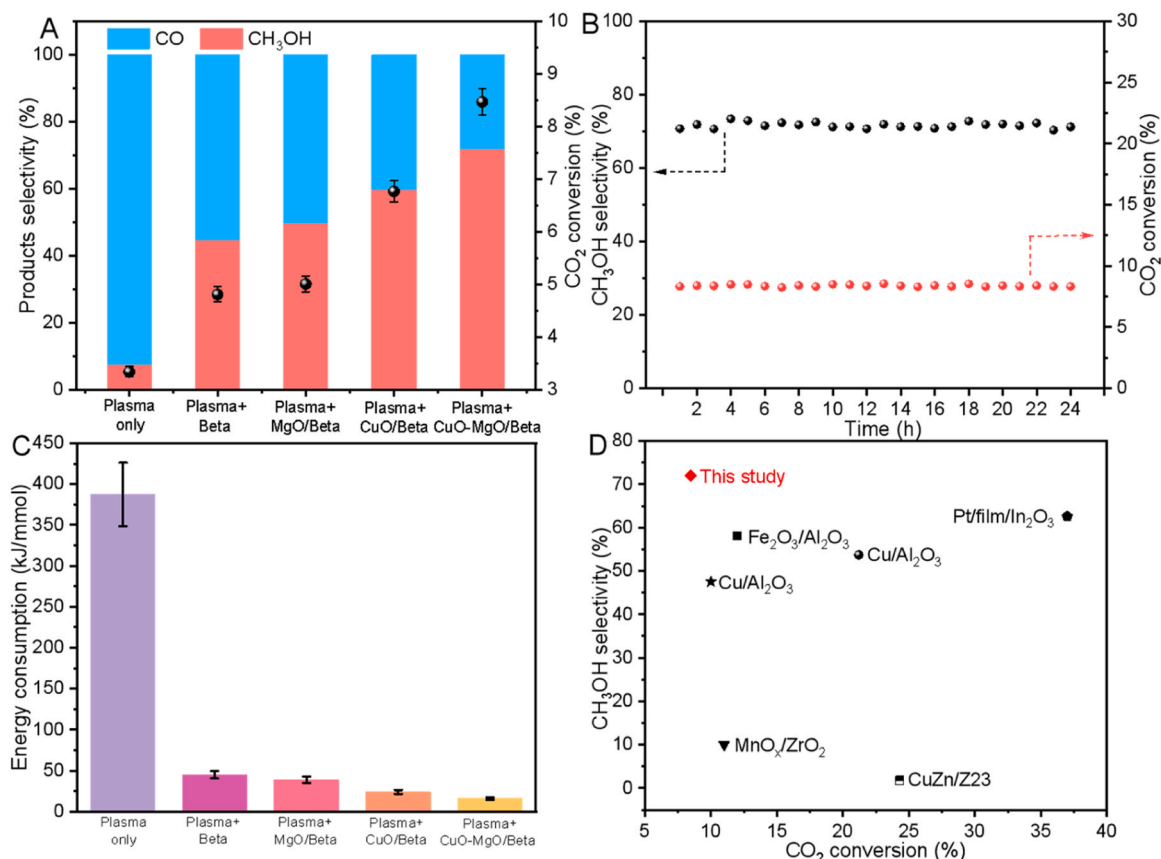


Fig. 1. Measured products selectivity and CO₂ conversion for CO₂ hydrogenation over CuO-MgO/Beta catalysts. (A) For plasma catalysis with plasma-only, plasma catalysis Beta, and plasma catalysis MgO/Beta (15Mg), and CuO/Beta (10Cu) and CuO-MgO/Beta (10Cu-15Mg) catalyst; (B) Stability test of the CuO-MgO/Beta (10Cu-15Mg) catalyst; (C) Energy consumption for CH₃OH generation: for plasma-only, plasma + Beta, plasma + MgO/Beta (15Mg), plasma + CuO/Beta (10Cu), and plasma + CuO-MgO/Beta (10Cu-15Mg); (D) A comparison about our results with some representative results from the literature for other plasma catalysis. (1.5 g catalyst, 9.2 kHz discharge frequency, 24 W input power, CO₂:H₂ = 1:3, WHSV = 2400 ml/g/h, 18 ml/min CO₂, 54 ml/min H₂, 30 °C circulating water).

role of active sites to promote CO_2 hydrogenation reaction. Interestingly, using the CuO-MgO/Beta (with 10 wt% Cu and 15 wt% Mg loading) catalyst, the performance has been dramatically improved up to 8.5% CO_2 conversion and 72.0% CH_3OH selectivity. These results demonstrate a clear synergistic effect between CuO and MgO in improving the performance of plasma-catalytic CO_2 hydrogenation to CH_3OH . This synergistic effect has also been observed over CuO-MgO/HX, CuO-MgO/MOR, CuO-MgO/S-1 and CuO-MgO/SSZ-13 catalysts, using HX, MOR, S-1 and SSZ-13 zeolites as support, respectively. However, CuO-MgO/Beta catalyst shows the best catalytic performance (Fig. S3).

In the CuO-MgO/Beta catalyst, the loading of MgO (with 10 wt% Cu loading) and the loading of CuO (with 15 wt% Mg loading) has been investigated (Fig. S4 A and B). The results show that the optimized loadings of Mg and Cu are 15 and 10 wt%, respectively. The optimization of the discharge power is shown in Fig. S5. Using the optimized CuO-MgO/Beta catalyst, the catalytic stability has been tested for 24 h (Fig. 1B), during which CO_2 conversion and CH_3OH selectivity remain stable at 8.5% and 72%, respectively, illustrating an excellent stability of CuO-MgO/Beta catalyst for plasma-catalytic CO_2 hydrogenation to CH_3OH .

Fig. 1C shows the energy consumption for CH_3OH production under different reaction conditions. It is clear that the energy consumption is significantly reduced by combining the plasma and the CuO-MgO/Beta catalyst since the energy consumption for “plasma only” is 387.5 kJ/mmol, but it drops to 17.9 kJ/mmol in the case of “plasma + CuO-MgO/

Beta”. This reduction in energy consumption by more than a factor of 20 indicates the key role of the synergy of CuO and MgO for efficient production of CH_3OH . Fig. 1D compares our results with some representative results from the literature driving CO_2 hydrogenation through plasma-catalysis but using different catalysts [13–18]. It can be seen that our catalyst i.e. CuO-MgO/Beta shows the best CH_3OH selectivity, although the CO_2 conversion is lower than that of the Pt-based catalyst [14].

3.2. Catalyst characterization

Fig. 2A shows the XRD patterns of MgO/Beta samples with varied Mg loading. It can be seen that no peaks of MgO species have been observed until the loading reaches 7%. That is, for the sample with 3% loading, Mg is highly dispersed on Beta zeolite, and thus it can not be observed by XRD. However, with rising Mg loading, the intensity of the peaks assigning to MgO gradually increase (PDF#87–0652), which indicates that MgO species was formed on Beta zeolite when the Mg loading is more than 7%. Fig. 2B shows the XRD patterns of the CuO-MgO/Beta samples with constant Cu loading (10%) but varied Mg loading. Clearly, the characteristic peaks of CuO (PDF#05–0661) have been observed, indicating the formation of CuO particles on the CuO-MgO/Beta samples. Interestingly, the intensity of characteristic peaks of MgO dramatically decreases for the CuO-MgO/Beta samples, in comparison with that of MgO/Beta samples in Fig. 2A with same Mg loading, which means that the co-loading of CuO and MgO has significantly

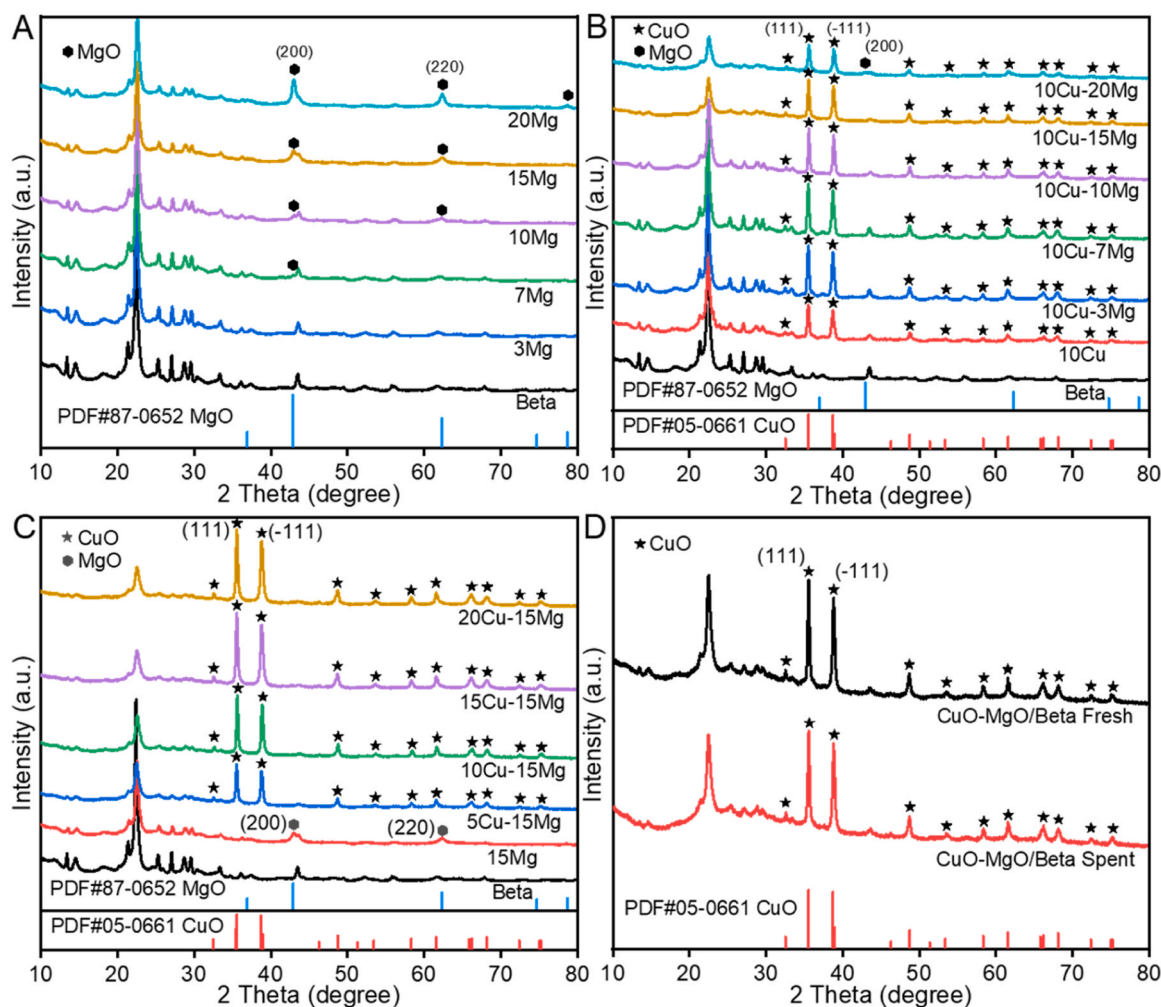


Fig. 2. XRD patterns of the catalysts. (A) MgO/Beta samples with varied Mg loading; (B) CuO-MgO/Beta samples with constant Cu loading (10%) but varied Mg loading; (C) CuO-MgO/Beta samples with constant Mg loading (15%) but varied Cu loading; (D) Fresh and spent CuO-MgO/Beta (10Cu-15Mg).

improved the dispersion of MgO on Beta zeolite. Fig. 2C shows the XRD patterns of the CuO-MgO/Beta samples with constant Mg loading (15%) but varied Cu loading. With the increase of Cu loading, the intensity of the XRD peaks assigning to CuO gradually rises, which may be caused by more and/or bigger CuO particles supported on Beta zeolite. In addition, in comparison with the sample MgO/Beta (15Mg), co-loading of CuO and MgO significantly lowers the intensities of the peaks of MgO species, which further demonstrate that CuO species improves the dispersion of MgO on Beta zeolite, implying a strong interaction between CuO and MgO species. For all of the CuO-MgO/Beta samples, the characteristic peaks of Beta zeolite are all present, which indicates that the crystalline structure of Beta zeolite has not been damaged after loading CuO and MgO. However, the intensity of the characteristic peaks of Beta have been weakened, which may be caused by covering of Beta surface by CuO and MgO species [19]. Fig. 2D shows the XRD patterns of the fresh and spent CuO-MgO/Beta catalyst. In general, the XRD result of the fresh and spent catalysts do not change significantly, indicating that the catalyst is stable. However, compared with the fresh sample, the intensity of CuO characteristic peaks of the spent CuO-MgO/Beta catalyst decreases slightly, which may be caused by partially reduction of CuO by H₂ during plasma-catalytic CO₂ hydrogenation reaction, which can be further confirmed by H₂-TPR and XPS results.

Fig. 3 shows the H₂-TPR profiles of the catalysts. In Fig. 3A, no H₂ consumption peak has been observed for the sample MgO/Beta (3Mg), which means that MgO can not be reduced under the temperature employed in H₂-TPR test. In Fig. 3B, a broad reduction peak with a shoulder has been observed for the sample CuO/Beta (10Cu). This broad peak can be deconvoluted into two obvious peaks (marked as α and β)

and a flat peak (marked as γ). Generally, when Cu is supported on zeolites, Cu species including isolated Cu²⁺/Cu⁺ ions, CuO_x clusters and bulk CuO particles can be formed [20–22]. In Fig. 3B, the peaks α and β are generally attributed to highly dispersed CuO_x clusters with weak and strong interaction with the Beta support, respectively. The peak γ is usually caused by reduction of bulk CuO particles [6]. As for the samples of the CuO-MgO/Beta with constant Cu loading (10%) but varied Mg loading, a new reduction peak at around 226 °C (denoted as peak θ) has been observed, and its intensity gradually increase with rising Mg loading, although Cu loading is constant. The peak θ is usually assigned to the reduction of dispersed Cu species directly interacts with MgO [6]. That is, high loading of Mg favors formation of CuO-MgO species with direct interaction between CuO and MgO. Meanwhile, with rising Mg loading, the intensity of peak α (CuO_x clusters with weak interaction with support) gradually decreases, but the peak β (CuO_x clusters with strong interaction with support) increases, which means that MgO enhances the interactions between CuO species and support (MgO and Beta). Fig. 3C illustrates the H₂-TPR profiles of the CuO-MgO/Beta samples with constant Mg loading (15%) but varied Cu loading. With rising Cu loading, the intensity of the reduction peaks assigning to Cu species (θ , α , β and γ) gradually increase, which means that high loading of Cu favors formation of more Cu species. However, the relative content of Cu species (θ , α , β and γ) vary obviously. Fig. 3D compares the H₂-TPR profiles of the fresh and spent CuO-MgO/Beta (10Cu-15Mg) catalyst. It can be seen that, for the spent sample, a new reduction peak appears at 325 °C (denoted as peak λ), which is usually attributed to reduction of Cu₂O to metallic Cu [23,24]. That is, during the plasma-catalytic CO₂ hydrogenation, a part of CuO has been partially reduced to form Cu₂O,

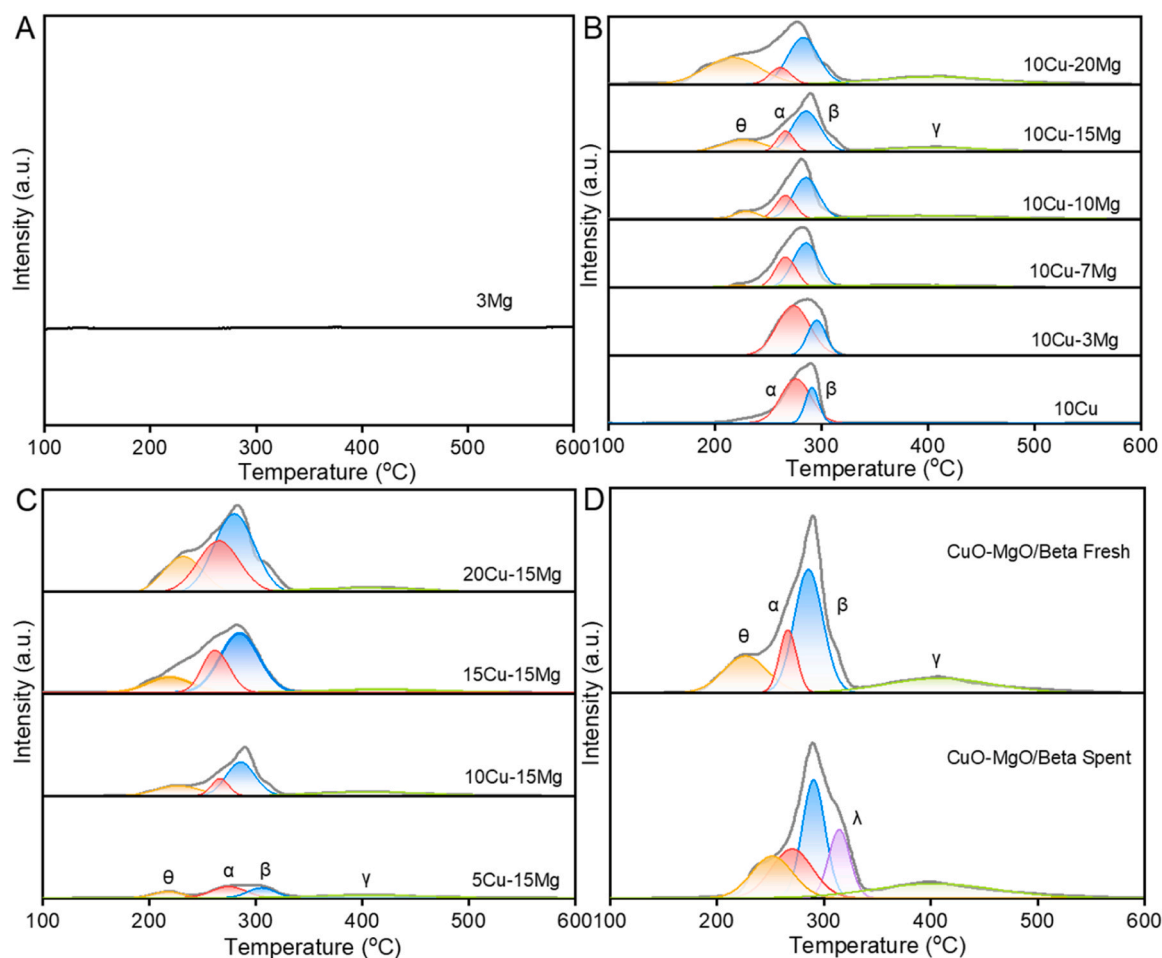


Fig. 3. H₂-TPR profiles of the catalysts. (A) MgO/Beta with 3% loading; (B) CuO-MgO/Beta samples with constant Cu loading (10%) but varied Mg loading; (C) CuO-MgO/Beta samples with constant Mg loading (15%) but varied Cu loading; (D) Fresh and spent CuO-MgO/Beta (10Cu-15Mg).

which is consistent with the XRD results.

Fig. 4A and B show the HRTEM images and particle size distribution of CuO for the samples CuO/Beta (10Cu) and CuO-MgO/Beta (10Cu-15Mg), respectively. It can be seen that the average particle sizes of CuO in the CuO/Beta and CuO-MgO/Beta are 3.69 and 3.47 nm, respectively. That is, CuO has been highly dispersed in the two sample, and MgO hardly changes the dispersion of CuO, which means that the improvement of catalytic performance in Fig. 1A from CuO/Beta to CuO-MgO/Beta may not be caused by change of CuO dispersion. Fig. 4C and D exhibit the HRTEM images of the CuO-MgO/Beta. Fig. 4C shows the obvious lattice fringe of MgO (220), and Fig. 4D shows the distinct lattice fringe of CuO (111) in the same region. This result demonstrates the interaction between MgO and CuO since they have directly combined with each other. This can be further proved by the fast Fourier transformation results in Fig. 4E, since the diffraction spots of MgO (220) and CuO (111) have been observed simultaneously in the same

region. Furthermore, the STEM-Mapping images in Fig. 4F indicate that Cu and Mg have been highly dispersed on Beta zeolite.

Fig. 5 exhibits the XPS results of the catalysts, and the standard charge was calibrated by C 1 s binding energy of 284.8 eV. Fig. 5A shows the Cu 2p_{3/2} spectra of the CuO-MgO/Beta samples with constant Cu loading (10%) but varied Mg loading. For the sample 10Cu, the peaks at 933.5, 936.2 and 944.1 eV have been observed through deconvolution, and they are attributed to Cu 2p_{3/2} of Cu⁺, Cu²⁺ and satellite peak of divalent Cu species (CuO and Cu²⁺ in the exchange state), respectively [25–27]. For the CuO-MgO/Beta samples, the binding energy of Cu⁺ barely changes. However, the binding energy of Cu²⁺ decreases from 936.2 to 935.6 eV, and the binding energy of the oscillating satellite peak also varies from 944.1 to 942.9 eV after loading MgO. The decreasing of binding energy demonstrates an obvious electron transfer from MgO to CuO caused by strong interaction between CuO and MgO [28], which can be seen in the HRTEM images (Fig. 4). That is,

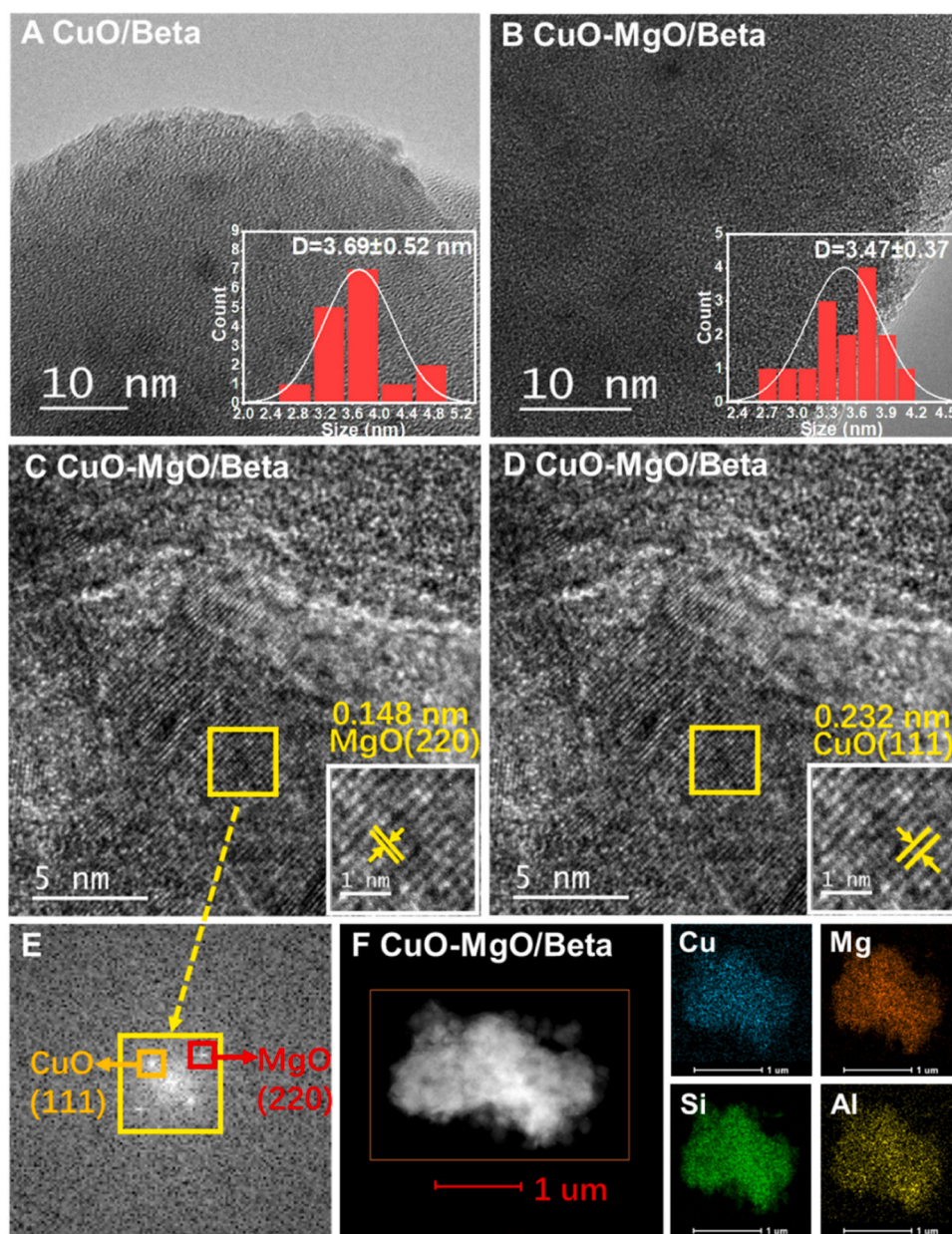


Fig. 4. HRTEM and STEM results of the catalysts. (A) HRTEM images and particle size distribution of CuO/Beta (10Cu); (B) HRTEM images and particle size distribution of CuO-MgO/Beta (10Cu-15Mg); (C) HRTEM images of CuO-MgO/Beta to show the lattice fringe of MgO (220); (D) HRTEM images of CuO-MgO/Beta to show the lattice fringe of CuO (111) in the same region; (E) fast Fourier transformation of the selected region in the HRTEM image to highlight interaction between MgO (220) and CuO (111); (F) STEM-Mapping images to show the distribution of Cu, Mg, Si and Al elements.

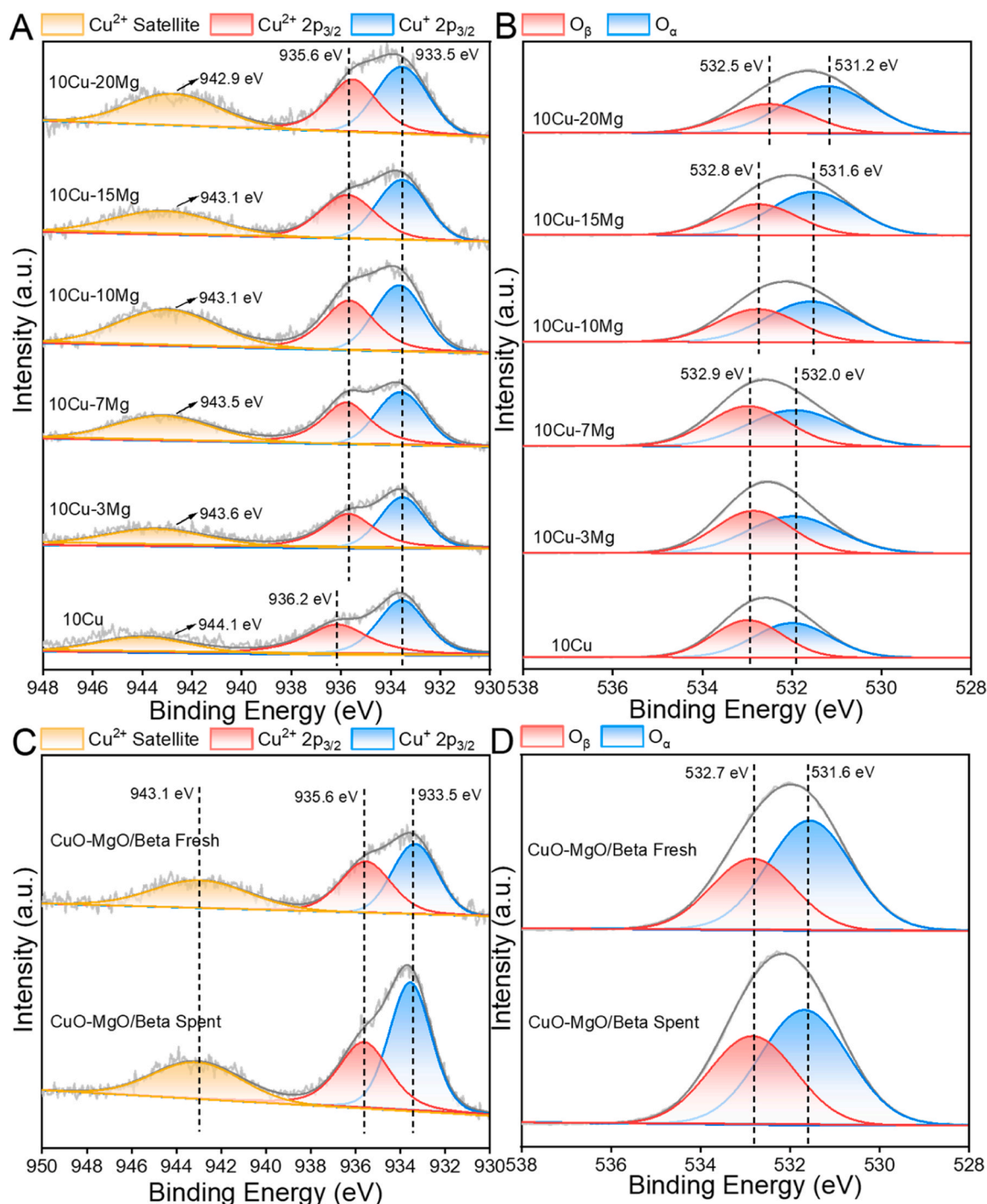


Fig. 5. XPS results of the catalysts. (A) Cu 2p_{3/2} spectra of the CuO-MgO/Beta samples with constant Cu loading (10%) but varied Mg loading; (B) O 1s spectra of the CuO-MgO/Beta samples with constant Cu loading (10%) but varied Mg loading; (C) Cu 2p_{3/2} spectra of the fresh and spent CuO-MgO/Beta (10Cu-15Mg) catalyst; (D) O 1s spectra of the fresh and spent CuO-MgO/Beta (10Cu-15Mg) catalyst. The standard charge was calibrated by C 1s binding energy of 284.8 eV.

co-loading of CuO and MgO results a strong interaction between CuO and MgO, which is favorable for partially reduction of CuO. In the O 1s spectra, two peaks at 532.0 and 532.9 eV have been observed in Fig. 5B, and they are assigned to lattice oxygen (O_{latt}) and adsorbed oxygen (O_{ads}) species, respectively [29]. Clearly, after loading Mg, the binding energy of both O_{latt} and O_{ads} decreases, which may also be caused by strong interaction between CuO and MgO. The XPS results of the Cu 2p_{3/2} and O 1s for fresh and spent CuO-MgO/Beta (10Cu-15Mg) catalyst are shown in Fig. 5C and D, respectively. It can be seen that, compared with the fresh catalyst, the relative content of Cu⁺ in the spent catalyst

increases greatly. This further indicates partially reduction of CuO to Cu₂O species during the reaction process, which is in consistent with the XRD and H₂-TPR results. However, the relative content of O_{latt} and O_{ads} species hardly change during the reaction process.

Cu (LMM) Auger peaks are traditionally used to distinguish Cu⁰, Cu⁺ and Cu²⁺ species since the kinetic energies of their Auger electrons are distinctive. Generally, Cu (LMM) Auger peaks of Cu⁰, Cu⁺ and Cu²⁺ are located at 918.7, 916.8 and 917.8 eV, respectively [30]. The Cu LMM result in Fig. S6 indicates that CuO is the main Cu species for the fresh CuO-MgO/Beta catalyst, but the intensity of Cu⁺ increases for the spent

CuO-MgO/Beta catalyst. That is, CuO has been partially reduced to form Cu₂O species during the reaction process, which is in consistent with the above-mentioned H₂-TPR and XPS results.

The interaction between CuO and MgO was characterized by the techniques described above. XRD patterns indicate that co-loading of CuO and MgO reduces the intensities of MgO peaks compared to MgO/Beta samples, suggesting enhanced MgO dispersion on Beta zeolites by CuO. H₂-TPR profiles demonstrate that increasing Mg loading results in a decrease in the α peak intensity and an increase in the β peak of CuO, highlighting the role of MgO in enhancing interactions between CuO species and the support. In addition, HRTEM images reveal direct combination between MgO (220) and CuO (111), further confirming their interaction. Furthermore, XPS indicated a clear electron transfer from MgO to CuO, which verifies the strong interaction between MgO and CuO.

To distinct the active sites of CuO-MgO/Beta catalyst for plasma-catalytic CO₂ hydrogenation to produce CH₃OH, the CuO-MgO/Beta catalyst was completely reduced to form metallic Cu⁰ species (Fig. S7A), which was then used for plasma-catalytic CO₂ hydrogenation. As shown in Fig. S7B, the reduced CuO-MgO/Beta catalyst shows much lower CO₂ conversion and CH₃OH selectivity than the fresh CuO-MgO/Beta catalyst, which means that metallic Cu⁰ species are not the active sites for plasma-catalytic CO₂ hydrogenation to produce CH₃OH. Therefore, these catalyst characterization results imply that Cu₂O species, coming from partially reduction of CuO during the reaction

process, are highly possible the active sites for plasma-catalytic CO₂ hydrogenation to produce CH₃OH. In addition, MgO plays a role of electron donor promoter, which is favorable for electron transfer from MgO to CuO, leading to easier reduction of CuO to form Cu₂O active sites.

Some other chemical composition and texture information of the catalysts can be found in Table S1 (chemical composition), Table S2 (specific surface area, pore volume and pore size), Fig. S8 (N₂ isothermal) and Fig. S9 (SEM images).

MgO is a basic oxide, while Beta zeolite is a solid acid. Therefore, the acid-base property of the CuO-MgO/Beta catalysts may be another important factor in determining the catalytic performance, and thus CO₂-TPD and NH₃-TPD have been employed to analyze the basic and acidic property, respectively. In Fig. 6A, the strength and amounts of basic sites on the catalysts are measured by CO₂-TPD. Three CO₂ desorption peaks (denote as α , β and γ) can be observed, and they correspond to weak, moderate and strong basic sites, respectively [31]. Clearly, the β and γ peaks hardly appear for the sample of Beta and 10Cu, which means that a certain amount of moderate and strong basic sites have been introduced by MgO species. Furthermore, the strength and quantity of weak basic sites do not change significantly, while the quantity of moderate basic sites as well as strong basic sites increases with the increase of MgO loading. That is, the loading of MgO does increase the surface basicity of the catalysts, and thus the adsorption of CO₂ has been promoted, which may be one of the reasons why catalytic

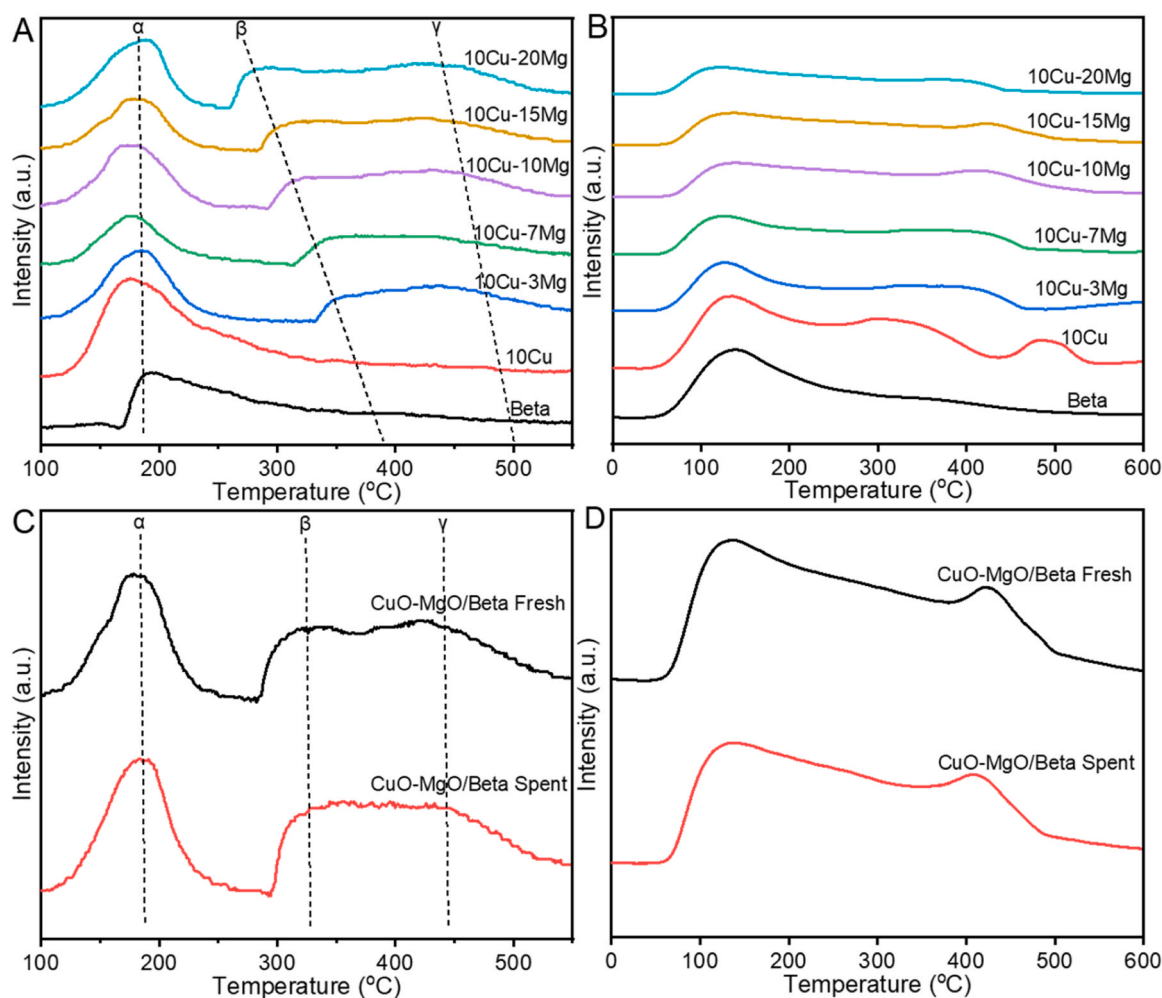


Fig. 6. CO₂-TPD and NH₃-TPD results of the catalysts. (A) CO₂-TPD results of the CuO-MgO/Beta samples with constant Cu loading (10%) but varied Mg loading; (B) NH₃-TPD results of the CuO-MgO/Beta samples with constant Cu loading (10%) but varied Mg loading; (C) CO₂-TPD of the fresh and spent CuO-MgO/Beta (10Cu-15Mg) catalyst; (D) NH₃-TPD results of the fresh and spent CuO-MgO/Beta (10Cu-15Mg) catalyst.

performance has been improved.

The acid sites of the catalysts are also investigated by NH_3 -TPD, as shown in Fig. 6B. The Beta support shows two NH_3 desorption peaks at 50–200 °C and 300–500 °C, which correspond to weak acid sites and moderate acid sites, respectively [32–35]. The sample 10Cu exhibits three NH_3 desorption peaks, corresponding to weak, moderate and strong acid sites. This may be caused by generation of new Lewis acid sites [36] derived from CuO on Beta [19] and substitution of Brönsted proton sites ($-\text{O}-\text{H}^{\delta+}$) on the Beta surface by Cu species. Subsequently, the acidity and the amount of total acid sites on the Beta gradually decrease with the increasing of MgO loading, since the acid sites of Beta is occupied by MgO species. As illustrated in Fig. 6C and D, the basic sites, basic amounts, acid sites and acid amounts of the CuO-MgO/Beta (10Cu-15Mg) catalyst hardly change after the reaction, further illustrating the stability of the CuO-MgO/Beta catalyst.

3.3. Plasma diagnoses

In situ optical emission spectroscopy (OES) was employed to detect the important species in the CO_2/H_2 plasma, as presented in Fig. 7 A. The CO_2/H_2 plasma in the absence of a catalyst or support shows the highest signal intensity, including several spectral lines and two spectral bands, i.e., the H_α line (656.3 nm, $3d^2D \rightarrow 2p^2P^0$) [37], two O atomic spectral lines (777.5 nm, $3s^5S^0 \rightarrow 3p^5P$; 844.7 nm, $3s^5S^0 \rightarrow 3p^3P$) [38, 39], a H_2 band (580–650 nm, $d^3\Pi_u \rightarrow a^3\Sigma_g^+$) and a CO band (450 nm \rightarrow 580 nm, $B^1\Sigma \rightarrow A^1\Pi$) [40]. These results indicate that H atoms and CO molecules are abundant in the plasma.

The signal intensity is obviously reduced after packing the support, which may be caused by the shielding effect [41]. The signal intensity is further weakened when the plasma was packed by MgO/Beta (15Mg), CuO/Beta (10Cu) or CuO-MgO/Beta (10Cu-15Mg). We can see from Fig. 7B that the MgO/Beta (15Mg) catalyst shows an obvious absorption peak for UV-light (200–400 nm) but a much lower absorption intensity for visible light (400–800 nm). Because all the lines and bands mentioned above are located in the range of visible light, it is reasonable to believe that the reduction of the OES intensity is caused not only by optical interference from the packed catalysts but also by the ability of the active sites to adsorb the reactive species. For CuO/Beta (10Cu), some absorption of visible light in combination with the UV-vis spectrum have been observed, which also explains the further reduction of the signal intensity. The CuO-MgO/Beta (10Cu-15Mg) catalyst corresponds to the lowest signal intensity, as evidenced by the UV-vis spectrum, which shows an obvious absorption of visible light. Besides, a

further decrease in the relative intensity of CO compared to CuO/Beta (10Cu) indicates that the loading of MgO is capable of further suppressing the production of CO through synergistic interaction with CuO. In addition, changes in the relative strength of the peaks in these five OES profiles correspond well with the product selectivity in Fig. 1A. The CO selectivity exceeds 90% in the case of plasma-only, while the CH_3OH selectivity significantly increases from 7.5% to 72% when the plasma was packed by CuO-MgO/Beta (10Cu-15Mg) catalyst.

The plasma discharge behaviors are diagnosed by a two-channel digital oscilloscope. As shown in Fig. S10, the Lissajous graph changes from a parallelogram-like shape (Plasma only) to an oval shape when the plasma was packed by CuO-MgO/Beta (10Cu-15Mg) catalysts, which implies a significant change in the discharge pattern from the typical filamentary behavior to a surface-mode behavior [42]. Even at the same input power (24 W), the actual power exists small differences for the different catalysts. This is attributed to the change in the equivalent capacitance of the system with packing by different materials. It is obtained that there is no significant change in the waveform of the voltage after loading CuO and MgO to Beta, as shown in Fig. S11A. As shown in Fig. S11B, the current waveform corresponding to different catalysts is gradually enhanced except for the case of plasma only, indicating that the loading of CuO and MgO on the Beta zeolite is more favorable to the surface discharges. At the same time, the CO_2 conversion and CH_3OH selectivity corresponding to these four catalysts progressively rises, which is consistent with the increasing discharge currents. That is, the stronger surface discharge indicates a better synergy between the plasma and the active site, favoring the CH_3OH production.

3.4. In situ FTIR and reaction mechanism

To elucidate the reaction mechanism of plasma-catalytic CO_2 hydrogenation to CH_3OH over CuO-MgO/Beta catalyst, the active intermediates on Beta support, CuO/Beta (10Cu), MgO/Beta (15Mg) and CuO-MgO/Beta (10Cu-15Mg) catalysts were examined using an in situ FTIR setup (Fig. S2). As shown in Fig. 8, the amount of carbonate on the catalyst surface gradually increases from Beta to MgO/Beta (15Mg) (1635 cm^{-1} , 1360 cm^{-1} and 1340 cm^{-1}) [43,44]. Moreover, for the MgO/Beta (15Mg) sample, many new carbonate absorption bands appear at 1523 , 1418 and 1318 cm^{-1} [44,45], indicating that MgO enhances the adsorption of CO_2 to form carbonate species, which is consistent with the result of CO_2 -TPD. In addition, the peak intensity of surface carbonates species gradually increases after plasma on as the reaction proceeds, implying the presence of carbonate species is not only

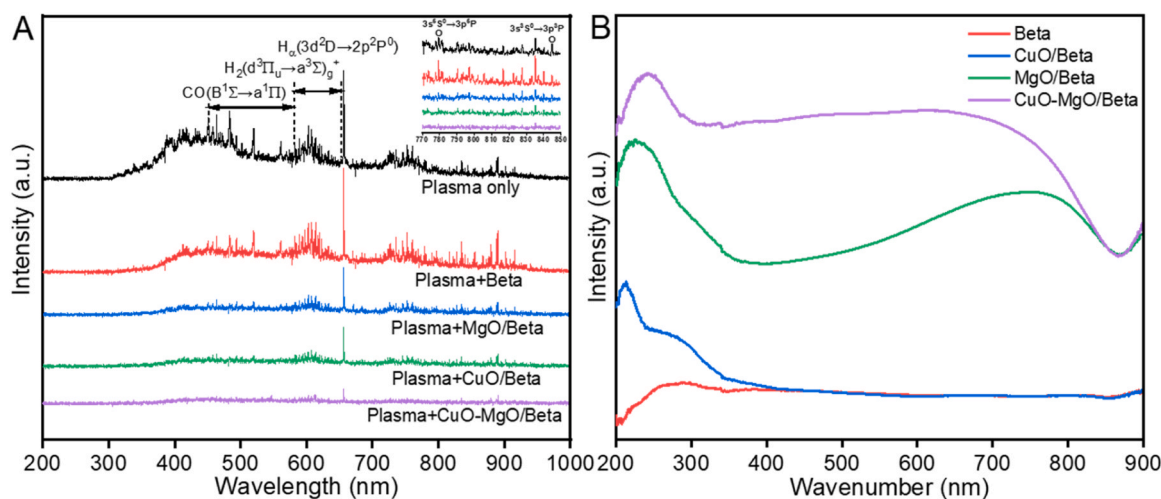


Fig. 7. (A) OES spectrum of the plasma-only, plasma catalysis Beta, and plasma catalysis MgO/Beta (15Mg), and CuO/Beta (10Cu) and CuO-MgO/Beta (10Cu-15Mg) catalyst; (B) UV-vis results of the plasma catalysis Beta, and plasma catalysis MgO/Beta (15Mg), and CuO/Beta (10Cu) and CuO-MgO/Beta (10Cu-15Mg) catalyst. (1.5 g catalyst, 9.2 kHz discharge frequency, 24 W input power, $\text{CO}_2/\text{H}_2 = 1:3$, WHSV = 2400 ml/g/h, 18 ml/min CO_2 , 54 ml/min H_2 , 30 °C circulating water).

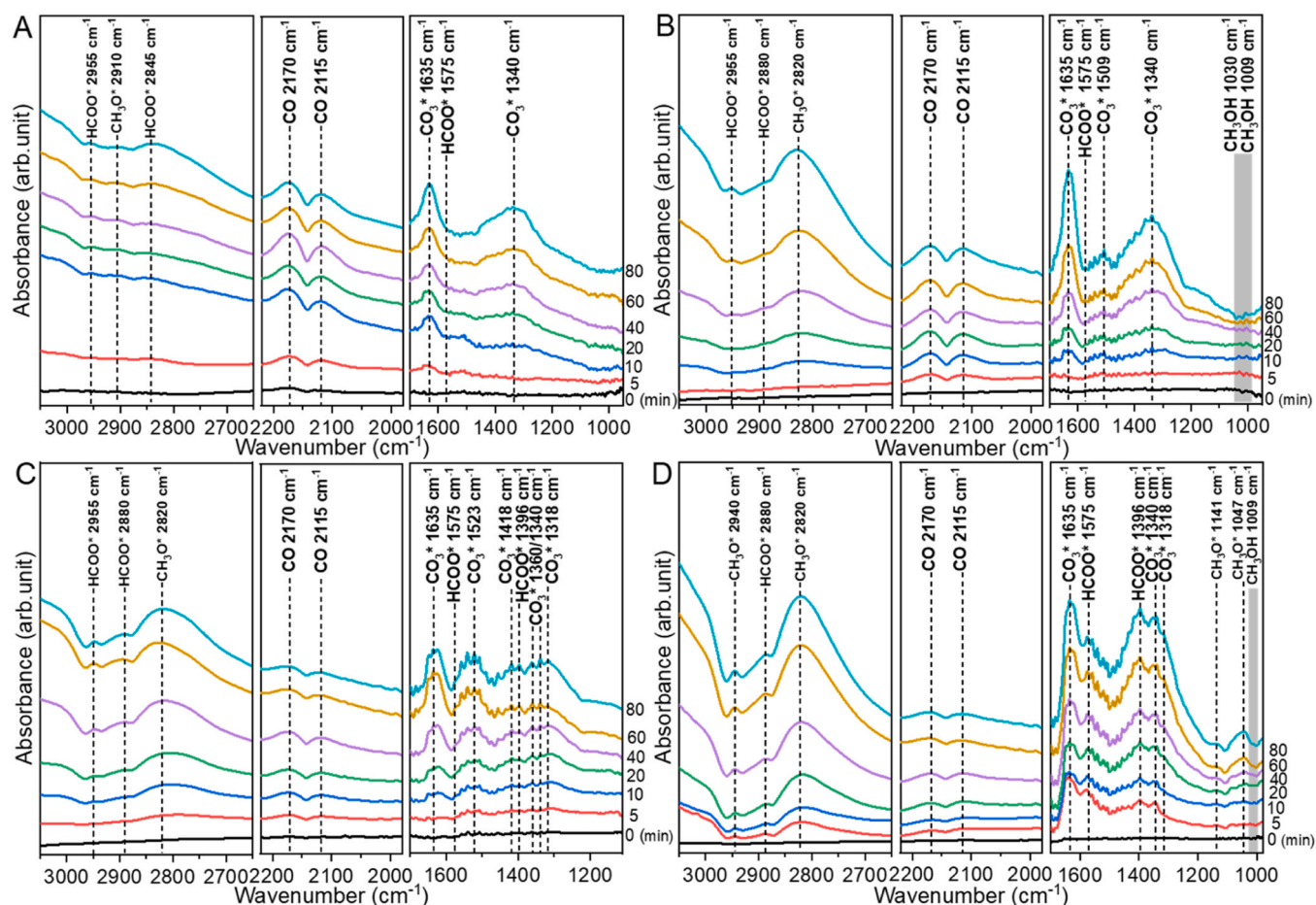


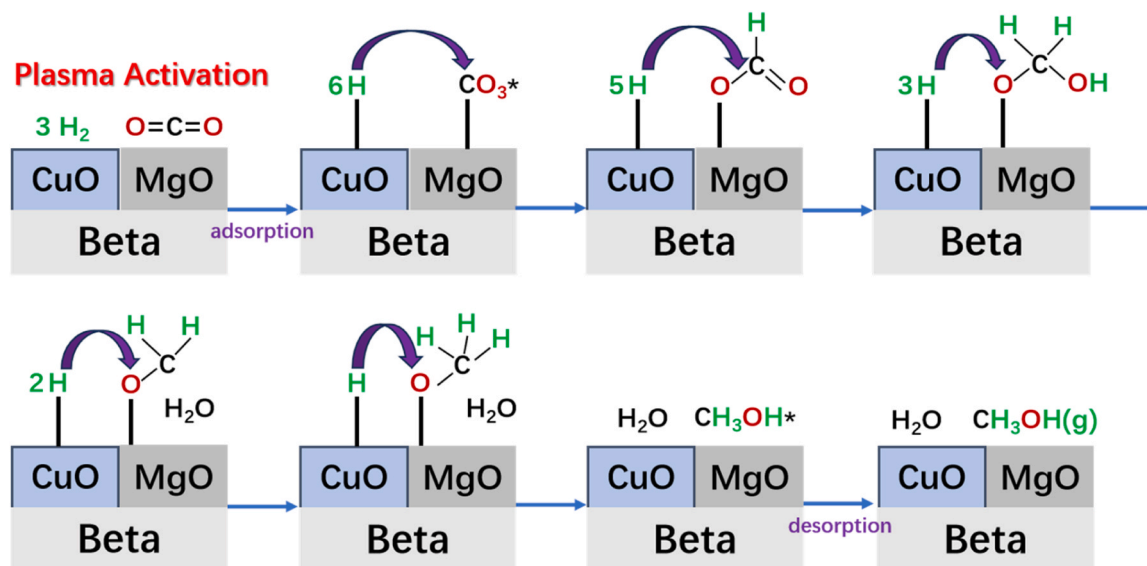
Fig. 8. In situ FTIR spectra of surface species on the catalysts. (A) Beta support; (B) CuO/Beta (10Cu) catalyst; (C) MgO/Beta (15Mg) catalyst; (D) CuO-MgO/Beta (10Cu-15Mg) catalyst. (18 ml/min CO_2 , 54 ml/min H_2 , 30 °C circulating water).

due to physical adsorption of CO_2 , but also attributed to plasma excitation, i.e., vibrational excitation of CO_2 adsorbed on the catalyst surface [44]. Comparing of MgO/Beta (15Mg) with CuO-MgO/Beta (10Cu-15Mg) demonstrates that the main species on the catalyst surface change from carbonate to formate and methoxy when Cu is present, since the peaks at 1523, 1418 and 1360 cm^{-1} disappear [42,43], but the intensity of the peaks at 2940, 2880, 2920, 1575 and 1396 cm^{-1} increase [44,46–49]. That is, the adsorbed CO_2 exists on the catalyst surface as carbonate on the surface with abundant MgO, and the carbonate is transformed into formate and methoxy intermediates in the presence of CuO and plasma. These formate and methoxy species may be further hydrogenated to form CH_3OH .

In Fig. 8, on the one hand, the intensity of the absorption bands of formate, methoxy and gas phase CH_3OH (1009 and 1030 cm^{-1}) gradually increases when CuO and MgO were co-loaded [48], which further demonstrates the synergistic role of CuO and MgO species on Beta for promoting CO_2/H_2 plasma reaction to produce CH_3OH [51]. On the other hand, the major species on the catalyst surface changes from formate to methoxy with co-loading of CuO and MgO (from 2955 to 2940 cm^{-1} and from 2845 to 2820 cm^{-1}) [44,47,49]. In particular, a new absorption band of methoxy at 1141 cm^{-1} and 1047 cm^{-1} appear in the case of CuO-MgO/Beta (10Cu-15Mg) [48,50], indicating that methoxy is a key intermediate for the formation of CH_3OH . Two bands at 2170 and 2115 cm^{-1} are attributed to absorbance of gas phase CO molecules [52,53]. The intensity of the CO absorption band significantly reduces from CuO/Beta (10Cu) to CuO-MgO/Beta (10Cu-15Mg), confirming that MgO does inhibit the production of CO. These CO absorbance bands decrease in intensity coincidentally with gradual increasing

in formate species absorption. These findings reveal a competitive mechanism between CO generation and formate species formation [52]. That is, MgO enhances the adsorption of CO_2 , resulting in the formation of a large number of carbonate species on catalyst surface. The carbonate species favor formation of formate rather than direct dissociation of CO_2 into CO in the presence of hydrogen and plasma. Thus, the selectivity of CH_3OH has been improved. However, MgO itself has shown poor reactivity, which can be evidenced by the MgO/Beta (15Mg) catalyst, as shown in Fig. 1A. The most likely explanation is that MgO is not effective in dissociating H_2 . Therefore, the introduction of CuO active sites that are known with more reactivity in dissociating H_2 would likely cooperate with their adjacent MgO sites (Fig. 4C), resulting in their synergy and boosting CH_3OH synthesis.

The possible reaction mechanism of CO_2 hydrogenation to CH_3OH over CuO-MgO/Beta catalyst driven by plasma is shown in Scheme 1. Overall, MgO sites prefer to adsorb CO_2 to form a substantial amount of carbonates, while CuO sites prefer to adsorb hydrogen species (activated H_2 molecule or H radicals produced by plasma) on the CuO-MgO/Beta catalyst. Subsequently, CuO sites and MgO sites synergistically collaborate to drive a series of hydrogenation steps, generating intermediate species such as HCOO and CH_2O . Finally, the critical precursor for CH_3OH formation, namely CH_3O , is generated, and it has been confirmed through in situ FTIR characterization. Therefore, we postulate the formate pathway for CH_3OH production from CO_2 hydrogenation: CH_3OH primarily emerges through a dual synergy, one between CuO and MgO sites within the catalyst and the other between the plasma and the CuO-MgO/Beta catalyst.



Scheme 1. Plausible reaction mechanism of CO₂ hydrogenation to CH₃OH over CuO-MgO/Beta catalyst driven by plasma. Highlighting the synergistic effects of CuO sites and MgO sites in promoting CO₂ hydrogenation through formate pathway. (The outermost Cu species exists as Cu₂O).

4. Conclusion

Using the CuO-MgO/Beta (10Cu-15Mg) catalyst, 72% CH₃OH selectivity with 8.5% CO₂ conversion have been achieved at atmospheric pressure (0.1 MPa) and room temperature (~30 °C). Catalyst characterization show the strong interaction between CuO and MgO, leading to the synergy between MgO and CuO species, which is responsible for the excellent selectivity of the CuO-MgO/Beta catalyst in plasma-catalytic CO₂ hydrogenation for CH₃OH production. Firstly, the strong interaction between CuO and MgO leads to electron transfer from MgO to CuO, which is favorable for partially reduction of CuO to form Cu₂O active sites. Secondly, MgO strongly adsorb CO₂ to form formate species, which not only promote CO₂ hydrogenation through formate pathway to produce CH₃OH, but also suppresses RWGS reaction to produce CO. This work is expected to provide valuable insights into the design of catalysts for efficient CO₂ hydrogenation.

CRediT authorship contribution statement

Qian Chen: Conceptualization, Validation, Formal analysis, Resources, Data curation, Writing – original draft, Writing – review & editing. **Shengyan Meng:** Conceptualization, Validation, Formal analysis, Resources, Data curation, Writing – original draft. **Rui Liu:** Validation, Formal analysis, Data curation. **Xiaohan Zhai:** Validation, Formal analysis, Data curation. **Xinkui Wang:** Resources, Data curation. **Li Wang:** Resources, Data curation. **Hongchen Guo:** Resources, Data curation. **Yanhui Yi:** Conceptualization, Validation, Formal analysis, Resources, Data curation, Writing – original draft, Writing – review & editing, Supervision, Funding acquisition.

Declaration of Competing Interest

The authors declare that they have no known competing financial interests or personal relationships that could have appeared to influence the work reported in this paper.

Data availability

Data will be made available on request.

Acknowledgements

We acknowledge financial support from the National Natural Science Foundation of China [21908016, 21978032] and the Fundamental Research Funds for the Central Universities of China [DUT18JC42].

Appendix A. Supporting information

Supplementary data associated with this article can be found in the online version at [doi:10.1016/j.apcatb.2023.123422](https://doi.org/10.1016/j.apcatb.2023.123422).

References

- [1] S. Kleiber, M. Pallua, M. Siebenhofer, S. Lux, Catalytic hydrogenation of CO₂ to methanol over Cu/MgO catalysts in a semi-continuous reactor, *Energies* 14 (2021) 4319, <https://doi.org/10.3390/en14144319>.
- [2] Y. Sun, Z. Lin, S.H. Peng, V. Sage, Z. Sun, A critical perspective on CO₂ conversions into chemicals and fuels, *J. Nanosci. Nanotechnol.* 19 (2019) 3097–3109, <https://doi.org/10.1166/jnn.2019.16588>.
- [3] F.T. Zangeneh, S. Sahebdehfar, M.T. Ravanchi, Conversion of carbon dioxide to valuable petrochemicals: An approach to clean development mechanism, *J. Nat. Gas. Chem.* 20 (2011) 219–231, [https://doi.org/10.1016/S1003-9953\(10\)60191-0](https://doi.org/10.1016/S1003-9953(10)60191-0).
- [4] S. Dang, B. Qin, Y. Yang, H. Wang, J. Cai, Y. Han, S. Li, P. Gao, Y. Sun, Rationally designed indium oxide catalysts for CO₂ hydrogenation to methanol with high activity and selectivity, *Sci. Adv.* 6 (2020) eaaz2060, <https://doi.org/10.1126/sciadv.aaz2060>.
- [5] C. Wang, Y. Fang, G. Liang, X. Lv, H. Duan, Y. Li, D. Chen, M. Long, Mechanistic study of Cu-Ni bimetallic catalysts supported by graphene derivatives for hydrogenation of CO₂ to methanol, *J. CO₂ Util.* 49 (2021), 101542, <https://doi.org/10.1016/j.jcou.2021.101542>.
- [6] T. Guo, Q. Guo, S. Li, Y. Hu, S. Yun, Y. Qian, Effect of surface basicity over the supported Cu-ZnO catalysts on hydrogenation of CO₂ to methanol, *J. Catal.* 407 (2022) 312–321, <https://doi.org/10.1016/j.jcat.2022.01.035>.
- [7] Z.L. Cui, C. Zhou, A. Jafarzadeh, X.X. Zhang, Y.P. Hao, L.C. Li, A. Bogaerts, SF₆ degradation in a γ-Al₂O₃ Packed DBD system: effects of hydration, reactive gases and plasma-induced surface charges, *Plasma Chem. Plasma P.* 43 (2023) 635–656, <https://doi.org/10.1007/s11090-023-10320-3>.
- [8] W. Liu, J. Baek, G.A. Somorjai, The methanol economy: methane and carbon dioxide conversion, *Top. Catal.* 61 (2018) 530–541, <https://doi.org/10.1007/s11244-018-0907-4>.
- [9] I. Ganesh, Conversion of carbon dioxide into methanol-a potential liquid fuel: Fundamental challenges and opportunities (a review), *Renew. Sust. Energ. Rev.* 31 (2014) 221–257, <https://doi.org/10.1016/j.rser.2013.11.045>.
- [10] A. Parastaev, W.F.L.M. Hoeben, B.E.J.M. van Heesch, N. Kosinov, E.J.M. Hensen, Temperature-programmed plasma surface reaction: An approach to determine plasma-catalytic performance, *Appl. Catal. B: Environ.* 239 (2018) 168–177, <https://doi.org/10.1016/j.apcatb.2018.08.011>.
- [11] H. Chen, Y. Mu, Y. Shao, S. Chansai, H. Xiang, Y. Jiao, C. Hardacre, X. Fan, Nonthermal plasma (NTP) activated metal-organic frameworks (MOFs) catalyst for

- catalytic CO₂ hydrogenation, *AIChE J.* 66 (2019), e16853, <https://doi.org/10.1002/aic.16853>.
- [12] D. Wierzbicki, M.V. Moreno, S. Ognier, M. Motak, T. Grzybek, P. Da Costa, M. E. Gálvez, Ni-Fe layered double hydroxide derived catalysts for non-plasma and DBD plasma-assisted CO₂ methanation, *Int. J. Hydrog. Energy* 45 (2020) 10423–10432, <https://doi.org/10.1016/j.ijhydene.2019.06.095>.
- [13] L. Wang, Y. Yi, H. Guo, X. Tu, Atmospheric pressure and room temperature synthesis of methanol through plasma-catalytic hydrogenation of CO₂, *ACS Catal.* 8 (2017) 90–100, <https://doi.org/10.1021/acscatal.7b02733>.
- [14] Z. Cui, S. Meng, Y. Yi, A. Jafarzadeh, S. Li, E.C. Neyts, Y. Hao, L. Li, X. Zhang, X. Wang, A. Bogaerts, Plasma-Catalytic Methanol Synthesis from CO₂ Hydrogenation over a Supported Cu Cluster Catalyst: Insights into the Reaction Mechanism, *ACS Catal.* 12 (2022) 1326–1337, <https://doi.org/10.1021/acscatal.1c04678>.
- [15] Y. Men, Y. Liu, Q. Wang, Z. Luo, S. Shao, Y. Li, Y. Pan, Highly dispersed Pt-based catalysts for selective CO₂ hydrogenation to methanol at atmospheric pressure, *Chem. Eng. Sci.* 200 (2019) 167–175, <https://doi.org/10.1016/j.ces.2019.02.004>.
- [16] X. Zhang, Z. Sun, Y. Shan, H. Pan, Y. Jin, Z. Zhu, L. Zhang, K. Li, Boosting methanol production via plasma catalytic CO₂ hydrogenation over a MnO_x/ZrO₂ catalyst, *Catal. Sci. Technol.* 13 (2023) 2529–2539, <https://doi.org/10.1039/d2cy02015g>.
- [17] M.Q. Feliz, I. Polaert, A. Ledoux, C. Fernandez, F. Azzolina-Jury, Influence of ionic conductivity and dielectric constant of the catalyst on DBD plasma-assisted CO₂ hydrogenation into methanol, *J. Phys. D.* 54 (2021), 334003, <https://doi.org/10.1088/1361-6463/abfddd>.
- [18] S. Meng, L. Wu, M. Liu, Z. Cui, Q. Chen, S. Li, J. Yan, L. Wang, X. Wang, J. Qian, H. Guo, J. Niu, A. Bogaerts, Y. Yi, Plasma-driven CO₂ hydrogenation to CH₃OH over Fe₂O₃/γ-Al₂O₃ catalyst, *AIChE J.* (2023), e18154, <https://doi.org/10.1002/aic.18154>.
- [19] S. Karnjanakom, A. Yoshida, A. Bayu, I. Kurnia, X. Hao, P. Maneechakr, A. Abudula, G. Guan, Bifunctional Mg-Cu-Loaded β-Zeolite: High Selectivity for the Conversion of Furfural into Monoaromatic Compounds, *ChemCatChem* 10 (2018) 3564–3575, <https://doi.org/10.1002/cctc.201800450>.
- [20] J. Yan, G. Lei, W.M.H. Sachtler, H. Kung, Deactivation of Cu/ZSM-5 Catalysts for Lean NO_x Reduction: Characterization of Changes of Cu State and Zeolite Support, *J. Catal.* 161 (1996) 43–54, <https://doi.org/10.1006/jcat.1996.0160>.
- [21] C. Torre-Abreu, M.F. Ribeiro, C. Henriques, G. Delahay, NO-TPD and H₂-TPR studies for characterisation of CuMOR catalysts, The role of Si/Al ratio, copper content and cocation, *Appl. Catal. B: Environ.* 14 (1997) 261–272, [https://doi.org/10.1016/S0926-3373\(97\)00028-3](https://doi.org/10.1016/S0926-3373(97)00028-3).
- [22] T. Beutel, J. Sárkány, G.-D. Lei, J.Y. Yan, W.M.H. Sachtler, Redox chemistry of Cu/ZSM-5, *J. Phys. Chem.* 100 (1996) 845–851, <https://doi.org/10.1021/jp952455u>.
- [23] W. Fu, C. Yin, Y. Feng, L. Zhang, F. Cheng, Z. Fang, C. Zhu, T. Tang, Synergistic catalysis of the Brønsted acid and highly dispersed Cu on the mesoporous Beta zeolite in the intermolecular aminooxidation of styrene, *Appl. Catal. A Gen.* 609 (2021), 117907, <https://doi.org/10.1016/j.apcata.2020.117907>.
- [24] J. Xue, X. Wang, G. Qi, J. Wang, M. Shen, W. Li, Characterization of copper species over Cu/SAPO-34 in selective catalytic reduction of NO_x with ammonia: Relationships between active Cu sites and de-NO_x performance at low temperature, *J. Catal.* 297 (2013) 56–64, <https://doi.org/10.1016/j.jcat.2012.09.020>.
- [25] B. Li, X. Luo, Y. Zhu, X. Wang, Immobilization of Cu (II) in KIT-6 supported Co₃O₄ and catalytic performance for epoxidation of styrene, *Appl. Surf. Sci.* 359 (2015) 609–620, <https://doi.org/10.1016/j.apsusc.2015.10.131>.
- [26] F. Li, L. Zhang, D.G. Evans, S. Duan, Structure and surface chemistry of manganese-doped copper-based mixed metal oxides derived from layered double hydroxides, *Colloid Surf. A* 244 (2004) 169–177, <https://doi.org/10.1016/j.colsurfa.2004.06.022>.
- [27] F. Bin, X. Wei, B. Li, K. Hui, Self-sustained combustion of carbon monoxide promoted by the Cu-Ce/ZSM-5 catalyst in CO/O₂/N₂ atmosphere, *Appl. Catal. B: Environ.* 162 (2015) 282–288, <https://doi.org/10.1016/j.apcatb.2014.07.007>.
- [28] L. Huang, F. Peng, F.S. Ohuchi, “In situ” XPS study of band structures at Cu₂O/TiO₂ heterojunctions interface, *Surf. Sci.* 603 (2009) 2825–2834, <https://doi.org/10.1016/j.susc.2009.07.030>.
- [29] J. Kim, E.E. Kwon, J.E. Lee, S.H. Jang, J.K. Jeon, J. Song, Y.K. Park, Effect of zeolite acidity and structure on ozone oxidation of toluene using Ru-Mn loaded zeolites at ambient temperature, *J. Hazard. Mater.* 403 (2021), 123934, <https://doi.org/10.1016/j.jhazmat.2020.123934>.
- [30] I. Platzman, R. Brenner, H. Haick, R. Tannenbaum, Oxidation of polycrystalline copper thin films at ambient conditions, *J. Phys. Chem. C* 112 (2008) 1101–1108, <https://doi.org/10.1021/jp076981k>.
- [31] C. Liu, X. Guo, Q. Guo, D. Mao, J. Yu, G. Lu, Methanol synthesis from CO₂ hydrogenation over copper catalysts supported on MgO-modified TiO₂, *J. Mol. Catal. A-Chem.* 425 (2016) 86–93, <https://doi.org/10.1016/j.molcata.2016.09.032>.
- [32] M. Anilkumar, W.F. Hölderich, Highly active and selective Nb modified MCM-41 catalysts for Beckmann rearrangement of cyclohexanone oxime to ε-caprolactam, *J. Catal.* 260 (2008) 17–29, <https://doi.org/10.1016/j.jcat.2008.08.019>.
- [33] D. Zhang, R. Wang, X. Yang, Beckmann rearrangement of cyclohexanone oxime over Al-MCM-41 and P modified Al-MCM-41 molecular sieves, *Catal. Commun.* 12 (2011) 399–402, <https://doi.org/10.1016/j.catcom.2010.11.006>.
- [34] C. Li, K. Fujimoto, Synthesis gas conversion to isobutane-rich hydrocarbons over a hybrid catalyst containing Beta zeolite - role of doped palladium and influence of the SiO₂/Al₂O₃ ratio, *Catal. Sci. Technol.* 5 (2015) 4501–4510, <https://doi.org/10.1039/c5cy00766f>.
- [35] J.H. Kim, M.J. Park, S.J. Kim, O.S. Joo, K.D. Jung, DME synthesis from synthesis gas on the admixed catalysts of Cu/ZnO/Al₂O₃ and ZSM-5, *Appl. Catal. A Gen.* 264 (2004) 37–41, <https://doi.org/10.1016/j.apcata.2003.12.058>.
- [36] S. Karnjanakom, A. Yoshida, W.B. Widayatno, A. Bayu, I. Kurnia, X. Hao, P. Maneechakr, A. Abudula, G. Guan, Selective deoxygenation of carboxylic acids to BTXs over Cu/β-zeolite prepared by ethylene glycol-assisted impregnation, *Catal. Commun.* 110 (2018) 33–37, <https://doi.org/10.1016/j.catcom.2018.03.002>.
- [37] G. Zambrano, H. Riascos, P. Prieto, E. Restrepo, A. Devia, C. Rincón, Optical emission spectroscopy study of r.f. magnetron sputtering discharge used for multilayers thin film deposition, *Surf. Coat. Tech.* 172 (2003) 144–149, [https://doi.org/10.1016/S0257-8972\(03\)00339-6](https://doi.org/10.1016/S0257-8972(03)00339-6).
- [38] A.V. Kholodkov, K.M. Golant, I.V. Nikolin, Nano-scale compositional lamination of doped silica glass deposited in surface discharge plasma of SPCVD technology, *Microelectron. Eng.* 69 (2003) 365–372, [https://doi.org/10.1016/S0167-9317\(03\)00323-X](https://doi.org/10.1016/S0167-9317(03)00323-X).
- [39] T. Czerwicz, J. Gavillet, T. Belmonte, H. Michel, A. Ricard, Determination of O atom density in Ar-O₂ and Ar-O₂-H₂ flowing microwave discharges, *Surf. Coat. Tech.* 98 (1998) 1411–1415, [https://doi.org/10.1016/S0257-8972\(97\)00256-9](https://doi.org/10.1016/S0257-8972(97)00256-9).
- [40] A. Granier, M. Vervloet, K. Aumaille, C. Vallee, Optical emission spectra of TEOS and HMDSO derived plasmas used for thin film deposition, *Plasma Sources Sci. Technol.* 12 (2003) 89–96, <https://doi.org/10.1088/0963-0252/12/1/312>.
- [41] Y. Yi, X. Wang, A. Jafarzadeh, L. Wang, P. Liu, B. He, J. Yan, R. Zhang, H. Zhang, X. Liu, H. Guo, E.C. Neyts, A. Bogaerts, Plasma-catalytic ammonia reforming of methane over Cu-based catalysts for the production of HCN and H₂ at reduced temperature, *ACS Catal.* 11 (2021) 1765–1773, <https://doi.org/10.1021/acscatal.0c04940>.
- [42] X. Zhang, Y. Liu, M. Zhang, T. Yu, B. Chen, Y. Xu, M. Crocker, X. Zhu, Y. Zhu, R. Wang, D. Xiao, M. Bi, D. Ma, C. Shi, Synergy between β-MoC Nanorods and Non-thermal Plasma for Selective CO₂ Reduction to CO, *Chem* 6 (2020) 3312–3328, <https://doi.org/10.1016/j.jcat.2019.02.021>.
- [43] C. Schild, A. Wokaun, On the mechanism of CO and CO₂ hydrogenation reactions on zirconia-supported catalysts: a diffuse reflectance FTIR, *Study, J. Mol. Catal.* 63 (1990) 243–254, [https://doi.org/10.1016/0304-5102\(90\)85147-A](https://doi.org/10.1016/0304-5102(90)85147-A).
- [44] J. Wang, G. Li, Z. Li, C. Tang, Z. Feng, H. An, H. Liu, T. Liu, C. Li, A highly selective and stable ZnO-ZrO₂ solid solution catalyst for CO₂ hydrogenation to methanol, *Sci. Adv.* 3 (2017), e1701290, <https://doi.org/10.1126/sciadv.1701290>.
- [45] A.G. Sato, D.P. Volanti, D.M. Meira, S. Damyanova, E. Longo, J.M.C. Bueno, Effect of the ZrO₂ phase on the structure and behavior of supported Cu catalysts for ethanol conversion, *J. Catal.* 307 (2013) 1–17, <https://doi.org/10.1016/j.jcat.2013.06.022>.
- [46] S. Xu, S. Chansai, S. Xu, C.E. Stere, Y. Jiao, S. Yang, C. Hardacre, X. Fan, CO Poisoning of Ru Catalysts in CO₂ Hydrogenation under Thermal and Plasma Conditions: A Combined Kinetic and Diffuse Reflectance Infrared Fourier Transform Spectroscopy-Mass Spectrometry Study, *ACS Catal.* 10 (2020) 12828–12840, <https://doi.org/10.1021/acscatal.0c03620>.
- [47] I.A. Fisher, A.T. Bell, In situ infrared study of methanol synthesis from H₂/CO₂ over Cu/SiO₂ and Cu/ZrO₂/SiO₂, *J. Catal.* 172 (1997) 222–237, <https://doi.org/10.1006/jcat.1997.1870>.
- [48] H. Zhao, R. Yu, S. Ma, K. Xu, Y. Chen, K. Jiang, Y. Fang, C. Zhu, X. Liu, Y. Tang, L. Wu, Y. Wu, Q. Jiang, P. He, Z. Liu, L. Tan, The role of Cu₁-O₃ species in single-atom Cu/ZrO₂ catalyst for CO₂ hydrogenation, *Nat. Catal.* 5 (2022) 818–831, <https://doi.org/10.1038/s41929-022-00840-0>.
- [49] W. Wang, Z. Qu, L. Song, Q. Fu, CO₂ hydrogenation to methanol over Cu/CeO₂ and Cu/ZrO₂ catalysts: Tuning methanol selectivity via metal-support interaction, *J. Energy Chem.* 40 (2020) 22–30, <https://doi.org/10.1016/j.jechem.2019.03.001>.
- [50] Y. Wang, W. Gao, H. Wang, Y. Zheng, W. Na, K. Li, Structure-activity relationships of Cu-ZrO₂ catalysts for CO₂ hydrogenation to methanol: interaction effects and reaction mechanism, *RSC Adv.* 7 (2017) 8709–8717, <https://doi.org/10.1039/c6ra28305e>.
- [51] J. Li, L. Dou, Y. Liu, Y. Gao, X. Hu, F. Yu, J. Li, S. Zhang, T. Shao, One-step plasma reforming of CO₂-CH₄ into hydrogen and liquid fuels: The roles of Cu and Fe sites on products distribution, *Fuel Process. Technol.* 242 (2023), 107648, <https://doi.org/10.1016/j.fuproc.2022.107648>.
- [52] L. Yao, X. Shen, Y. Pan, Z. Peng, Synergy between active sites of Cu-In-Zr-O catalyst in CO₂ hydrogenation to methanol, *J. Catal.* 372 (2019) 74–85, <https://doi.org/10.1016/j.jcat.2019.02.021>.
- [53] C. Vogt, E. Groeneveld, G. Kamsma, M. Nachtegaal, L. Lu, C.J. Kiely, P.H. Berben, F. Meirer, B.M. Weckhuysen, Unravelling structure sensitivity in CO₂ hydrogenation over nickel, *Nat. Catal.* 1 (2018) 127–134, <https://doi.org/10.1038/s41929-017-0016-y>.